MOLECULAR ENVIRONMENT AND THERMAL X-RAY SPECTROSCOPY OF THE SEMICIRCULAR YOUNG COMPOSITE SUPERNOVA REMNANT 3C 396

Yang $Su^{1,2}$, Yang $Chen^{2,3,7}$, Ji $Yang^{1,4}$, Bon-Chul Koo^5 , Xin $Zhou^2$, Deng-Rong Lu^1 , Il-Gyo $Jeong^5$, and $Tracey Delaney^6$

 $^{\rm 1}$ Purple Mountain Observatory, Chinese Academy of Sciences, Nanjing 210008, China Department of Astronomy, Nanjing University, Nanjing 210093, China

³ Key Laboratory of Modern Astronomy and Astrophysics, Nanjing University, Ministry of Education, Nanjing 210093, China
 ⁴ Key Laboratory of Radio Astronomy, Chinese Academy of Sciences, Nanjing 210008, China
 ⁵ Astronomy Program, Department of Physics and Astronomy, Seoul National University, Seoul 151-747, Korea
 ⁶ Kavli Institute for Astrophysics and Space Research, Massachusetts Institute of Technology, 70 Vassar Street, Cambridge, MA 02139,

USA Draft version October 30, 2018

ABSTRACT

We have investigated the molecular environment of the semicircular composite supernova remnant (SNR) 3C 396 and performed a Chandra spatially resolved thermal X-ray spectroscopic study of this young SNR. With our CO millimeter observations, we find that the molecular clouds (MCs) at $V_{\rm LSR} \sim 84~{\rm km~s^{-1}}$ can better explain the multiwavelength properties of the remnant than the $V_{\rm LSR} = 67-72~{\rm km~s^{-1}}$ MCs that are suggested by Lee et al. (2009). At around $84~{\rm km~s^{-1}}$, the western boundary of the SNR is perfectly confined by the western molecular wall. The CO emission fades out from west to east, indicating that the eastern region is of low gas density. In particular, an intruding finger/pillar-like MC, which may be shocked at the tip, can well explain the X-ray and radio enhancement in the southwest and some infrared filaments there. The SNR-MC interaction is also favored by the relatively elevated $^{12}CO J = 2-1/J = 1-0$ line ratios in the southwestern "pillar tip" and the molecular patch on the northwestern boundary. The redshifted 12 CO (J=1-0 and J=2-1) wings (86–90 km s⁻¹) of an eastern 81 km s⁻¹ molecular patch may be the kinematic evidence for shock–MC interaction. We suggest that the 69 km s⁻¹ MCs are in the foreground based on HI self-absorption while the 84 km s⁻¹ MCs at a distance of 6.2 kpc (the tangent point) are in physical contact with SNR 3C 396. The X-ray spectral analysis suggests an SNR age of ~ 3 kyr. The metal enrichment of the X-ray emitting gas in the north and south implies a $13-15M_{\odot}$ B1-B2 progenitor star.

Subject headings: ISM: individual (3C 396, G39.2-0.3) - ISM: molecules - supernova remnants

1. INTRODUCTION

The progenitors of core-collapse supernovae are massive stars and they most likely formed in giant molecular clouds (MCs). Because of their short lifetime, one may expect that the supernova remnants (SNRs) of corecollapse supernovae would be near their natal environment. The association with MCs often makes SNRs display irregular morphologies in multiwavelengths, which indicates complicated shock interaction with the complex, inhomogeneous ambient interstellar medium (ISM).

3C 396 (G39.2-0.3) is a semicircular young composite SNR, exhibiting both the central X-ray bright pulsar wind nebula (PWN) and western incomplete half-shell structures in multiwavelengths. In the high dynamicrange VLA images of the remnant, a remarkable "tail" extending from the very faint eastern shell of the SNR is revealed and is interpreted as an eastern "blow-out" structure (Patnaik et al. 1990). From VLA 6 and 20 cm data, a large scale brightness asymmetry is found in the east-west direction across SNR 3C 396, the western half of the remnant having roughly twice the flux density of the east (Anderson & Rudnick 1993). The Einstein Xray emission is bright in the limb and the center of the remnant (Becker & Helfand 1987). Based on ASCA X-

ray spectral analysis, a nonthermal component in the center of 3C 396 is attributed to a synchrotron PWN (Hurrus & Slane 1999). Recently, with about 100 ks high spatial resolution Chandra observation, a nonthermal nebula containing a point-like source is also found in the center of the remnant and is interpreted as a synchrotron PWN surrounding a yet undetected pulsar (Olbert et al. 2003). The possibility of the excess microwave emission arising from a spinning dust component toward 3C 396 is investigated at 33 GHz with the Very Small Array (VSA) telescope (Scaife et al. 2007). Based on the detection of H₂ molecules and the sharp southwestern boundary in the radio emission, the remnant is suggested to be encountering a MC in this region (Lee et al. 2009). The remnant is suggested at a distance of about 8.5 kpc because a cavity-like structure of the $V_{\rm LSR} \sim 69~{\rm km~s}^{-1}$ molecular gas seems to surround the remnant. The Spitzer IRS observation reveals that, along the western shell, the inner [FeII]-line filament and the outer H₂-line one is found to be spatially separated (Hewitt et al. 2009), which is similar to the result of near-IR 1.64 μm [FeII] and 2.12 μm H₂ line observations using Wide-field Infrared Camera aboard the Palomar 5 m Hale telescope (Lee et al. 2009). It is most probably because of the various molecular gas density conditions of the multi-phase preshock ISM across the western shell of 3C 396, where the shock of the remnant is interact-

 $^{^{7}}$ Corresponding author to whom any correspondence should be addressed.

ing with a complicated distribution of MCs (Hewitt et al. 2009). A detailed investigation of the molecular gas environment and the hot gas interaction with it are thus necessary, which may be helpful to understand the multiwavelength physical properties and the dynamic evolution of this irregularly shaped SNR.

In this paper, we have presented our millimeter CO line observations toward SNR 3C 396 and a spatially resolved Chandra thermal X-ray analysis. The observations and the data reduction are described in Section 2. The main observational results and calculations are presented in Section 3. The discussion and conclusions are given in Section 4 and Section 5, respectively.

2. OBSERVATIONS AND DATA REDUCTION

The observation was first made in the ^{12}CO (J=1–0) line (at 115.271 GHz) in 2006 April using the 6 m millimeter-wavelength telescope of the Seoul Radio Astronomy Observatory (SRAO) with single-side band filter and the 1024-channel autocorrelator with 50 MHz bandwidth. The half-power beam size at 115 GHz is 2' and the typical rms noise level was about 0.2 K at the 0.5 km s⁻¹ velocity resolution. The radiation temperature is determined by $T_{\rm R} = T_{\rm A}/(f_{\rm b} \times \eta_{\rm mb})$, where $T_{\rm A}$ is the antenna temperature, $f_{\rm b}$ the beam filling factor (assuming $f_{\rm b} \sim 1$), and $\eta_{\rm mb}$ the main beam efficiency ($\sim 75\%$). We mapped the 14' × 15' area covering 3C 396 centered at (19 $^{\rm h}04^{\rm m}06^{\rm s},05^{\circ}27'00''$) with grid spacing of $\sim 1'$.

The follow-up observations were made simultaneously in the $^{12}\mathrm{CO}$ $(J{=}1{-}0)$ line (at 115.271 GHz), $^{13}\mathrm{CO}$ $(J{=}1{-}0)$ line (110.201 GHz), and $\mathrm{C^{18}O}$ $(J{=}1{-}0)$ line (109.782 GHz) during 2008 November–December using the 13.7 m millimeter-wavelength telescope of the Purple Mountain Observatory at Delingha (hereafter PMOD). The spectrometer has 1024 channels, with a total bandwidth of 145 MHz (43 MHz) and the velocity resolution of 0.5 km s $^{-1}$ (0.2 km s $^{-1}$) for $^{12}\mathrm{CO}(^{13}\mathrm{CO})$ and $\mathrm{C^{18}O}$). The mean rms noise level of antenna temperature was less than 0.1 K for those lines. The intensity of the $\mathrm{C^{18}O}$ $(J{=}1{-}0)$ emission is too weak to examine its spatial distribution. The half-power beamwidth of the telescope is about 54" and the main beam efficiency η_{mb} was 52%. We mapped the 9' \times 9'.5 area centered at $(19^{\mathrm{h}}04^{\mathrm{m}}03^{\mathrm{s}},05^{\circ}26'30'')$ with grid spacing of 30".

We also made the $^{12}\mathrm{CO}$ (J=2-1) line observation toward partial regions of the SNR with grid spacing of 30" in 2010 February using the telescope of the SRAO to complement the data. The half-power beam size at 230 GHz is 48", the main beam efficiency was $\sim 57\%$, and the typical rms noise level was about 0.2 K at the 0.13 km s⁻¹ velocity resolution. The resolution of the SRAO $^{12}\mathrm{CO}$ (J=2-1) observation and the PMOD $^{12}\mathrm{CO}$ (J=1-0) observation are very similar, which makes it convenient to directly compare the two observations.

All the CO observation data were reduced using the GILDAS/CLASS package developed by IRAM.²

The Chandra X-ray and Spitzer 24 μ m mid-IR observations are also used for analysis. We revisited the Chandra ACIS observational data of SNR 3C 396 (ObsIDs: 1988; PI: S. P. Reynolds) with total exposure time

of about 100 ks. We reprocessed the event files (from Level 1 to Level 2) using the CIAO3.4 data processing software to remove pixel randomization and to correct for CCD charge-transfer inefficiencies. The overall light curve was examined for possible contamination from a time-variable background. The reduced data, with a net exposure of 93.7 ks, were used for our subsequent analysis. The mid-IR 24 μm observation used here was carried out as the 24 and 70 Micron Survey of the Inner Galactic Disk Program (PID: 20597; PI: S. Carey) with the Multiband Imaging Photometer (MIPS) (Rieke et al. 2004). The Post Basic Calibrated Data (PBCD) of the 24 μ m mid-IR were obtained directly from Spitzer archive. The VLA 1.4 GHz radio continuum emission (L band) data were adopted from Anderson & Rudnick (1993). The HI-line data and the large scale ¹³CO line data were obtained from the archival VLA Galactic Plane Survey (VGPS: Stil et al. 2006) and the Galactic Ring Survey (GRS: Jackson et al. 2006), respectively.

3. RESULTS

3.1. Molecular Gas Environment of SNR 3C 396

The large field of view $(14' \times 15')^{-12}$ CO channel maps are made with the SRAO observation and shown in Figures 1 and 2, overlaid with radio (red thick) and X-ray (cyan thin) contours. The velocity components around 69 km s $^{-1}$ (in 64–72 km s $^{-1}$ interval) and around 84 km s^{-1} (in $80-88 \text{ km s}^{-1}$ interval) both seem to have positional correlations with SNR 3C 396. The 69 km s⁻¹ MCs are mainly situated in the north of the remnant [with the $64-67 \text{ km s}^{-1}$ molecular gas in the northeast and the 68–71 km s⁻¹ gas in the northwest (NW)]. The SNR seems to be projected roughly within a cavity-like structure of the ¹²CO 69 km s⁻¹ component (Figure 1). However, the morphology of the 69 km s⁻¹ component appears to not well match the radio boundary of the remnant; especially, the $68-71~\mathrm{km~s^{-1}}$ gas appears to overlap the northwestern corner of the remnant. On the other hand, at around 84 km s⁻¹ (Figure 2), a thick wall structure of molecular gas is seen in the west; the eastern face of the wall at the 85–87 km s⁻¹ interval perfectly follows the western radio boundary of the remnant. The radio contours of the remnant seem to coincide with a cavity at $85-87 \,\mathrm{km}\,\mathrm{s}^{-1}$. The CO emission around 84 km s⁻¹ and the remnant's radio emission both seem to fade out gradually from west to east.

These characteristics are seen more clearly in the close-up image (Figure 3, left panel) made from the PMOD observation with a higher resolution. As also shown in Figure 3 (left panel), the X-ray/mid-IR/radio emission in the west of the remnant appears to be well confined by the western molecular wall around 84 km s⁻¹. Moreover, a prominent finger/pillar-like MC is seen in the southwest (SW), with one end intruding inside the SNR border. The radio and IR brightness peaks of the remnant are located at the short southwestern section of shell that "cuts" the molecular pillar. Also in the southwestern edge, an X-ray enhancement is coincident with the radio peak; in Section 3.2 below, we will show that this X-ray enhancement is exceptionally soft and of normal metal abundance.

As an attempt to remove the confusion by large-scale density gradient, we used the unsharp masking method

² http://www.iram.fr/IRAMFR/GILDAS

as described in Landecker et al. (1999), in which we subtracted the smoothed ¹²CO intensity map from the original ¹²CO map. Similar images can also be produced by subtracting the smoothed and scaled ¹³CO intensity image from original ¹²CO image. In the "cleaned" image of the $69~{\rm km~s^{-1}}$ MCs, the cavity-like structure is seen again (Figure 4, the right panel in the first line), but it clearly does not well match the radio boundary of the remnant. For the 84 km s⁻¹ MCs, on the other hand, the southwestern finger/pillar-like intrusion and the western molecular wall can be seen clearer in the "cleaned" image (Figure 4, the right panel in the second line) than in the intensity maps. The western boundary of the SNR appears to perfectly follow the left side of a molecular wall again (Figure 4, the right panel in the third line). A patch of strong ¹²CO emission around 84 km s⁻¹ is seen in the NW, where the radio emission of the SNR is slightly enhanced; this patch can also be discerned in the channel map, Figure 2, at $84\,\mathrm{km\,s^{-1}}$. In addition, there is another patch of ^{12}CO emission in 87–90 km s⁻¹ interval in the eastern "blow-out" region of the remnant (Figure 4, the right panel in the fourth line); it can also be discerned in Figure 2 at $87-88 \text{ km s}^{-1}$.

The integrated CO-line intensity ratio between the different transitions is suggested as a probe of the SNR-MC interaction (Seta et al. 1998; Jiang et al. 2010). The 12 CO J= 2-1/J= 1-0 ratio maps towards 3C396 at 66.5-68, 68-70.5, 70.5-72, 80-83, 83-85, and 85- $88\,\mathrm{km}\,\mathrm{s}^{-1}$ (which covers the centers and wings of the $69 \text{ and } 84 \,\mathrm{km}\,\mathrm{s}^{-1}$ lines, respectively) are presented in Figure 5. For the $\sim 84\,\mathrm{km\,s^{-1}}$ component, the ratios are clearly elevated to as high as > 0.9 in 80-83 km s⁻¹ interval (compared with ~ 0.5 –0.7 in average) in the southwestern molecular intrusion region and the northwestern molecular patch (corresponding to the two radio brightness peaks, respectively) described above. For the $\sim 69 \,\mathrm{km \, s^{-1}} \, (66.5 - 72 \,\mathrm{km \, s^{-1}})$ component, although the ratios are weakly elevated in some boundary regions, the ratios are all below 0.9. Therefore the elevated $^{12}CO\ J=$ 2-1/J=1-0 ratios seem to better imply an interaction of the SNR with the $\sim 84\,\mathrm{km\,s^{-1}}$ MCs than with the $\sim 69 \, \mathrm{km \, s^{-1}}$ ones.

We have carefully examined the CO spectra in the field of view and presented the $^{12}CO(J = 1-0)$, $^{12}CO(J = 2-$ 1), and ${}^{13}CO(J = 1-0)$ spectra extracted from two regions (in the east and SW, as marked in the right panel in the fourth line of Figure 4) in Figure 6. Around $69 \,\mathrm{km} \,\mathrm{s}^{-1}$, the $^{13}\mathrm{CO}$ line profiles are very similar to the ¹²CO profiles for both the "East" and "SW" regions. Both the ¹²CO and ¹³CO spectra of the "SW" region have peaks at 84 km s⁻¹, with broad blue (left) wings in the line profiles. Yet, it is difficult to judge whether the blue wings of the 84 km s^{-1} ¹²CO lines are dynamically broadened or not, due to the significant blue wing of the ¹³CO line and especially a distinct ¹³CO peak at 81 km s⁻¹. ¹³CO emission is usually optically thin and indicative of quiescent, intrinsically high-columndensity MCs. For the "East" region, both the ¹²CO and ¹³CO spectra have peaks at 81 km s⁻¹; notably, there is an additional broadening in the red (right) wing $(86-90 \text{ km s}^{-1})$ of the 81 km s⁻¹ ¹²CO line, as compared with little ¹³CO emission in the same velocity interval. It most likely indicates that the $^{12}\mathrm{CO}$ emission in this interval results from the perturbation suffered by the 81 km s⁻¹ molecular gas in the east of the remnant. Although there is a velocity discrepancy between 81 km s⁻¹ for the eastern region and 84 km s⁻¹ for the western region, the undisturbed clouds in the SNR field may have a wide velocity distribution, e.g., the LSR velocity of MCs with which SNR IC 443 interacts is in the range of -7 to $-2\,\mathrm{km\,s^{-1}}$ (van Dishoeck et al. 1993; Hewitt et al. 2006). Thus the 81 km s⁻¹ cloud in the east is very likely, together with the 84 km s⁻¹ clouds, among the MCs shocked by SNR 3C 396.

The above analysis show that both of the 69 and 84 km s⁻¹ molecular components appear to have spatial correlation with SNR 3C 396, but the latter seems to have much better evidence than the former. We will further show that the 69 km s⁻¹ clouds are in the foreground of SNR 3C 396, using the VGPS radio and GRS $^{13}{\rm CO}$ data.

The 1420 MHz continuum image (Figure 7, upper left panel) displays semicircularly brightened structure in the side roughly close to the Galactic plane and faint emission in another side. Following the method used in Tian et al. (2007), we produced the HI spectrum (Figure 7, upper right panel) of the radio peak region of the remnant. The maximum radial velocity of absorption features in the direction towards 3C 396 is up to the tangent point LSR velocity (i.e., $\sim 84 \text{ km s}^{-1}$), and virtually no significant absorption feature appears at negative velocities. It indicates that the distance of SNR 3C 396 is between 6.2 kpc (the tangent point) and 12.5 kpc (the Solar circle). Here we have used the rotation curve in Clemens (1985) with $R_0 = 8.0$ kpc (Reid 1993) and $V_0 = 220 \text{ km s}^{-1}$ and adopted the spiral model in Taylor & Cordes (1993; Figure 1 therein).

The HI self-absorption (SA) measurement can provide another clue to the MCs' distances. A single radial velocity indicates two distances (the near and the far kinematic distances) in the inner Galaxy along the line-ofsight (LOS). MCs in the near distance often display HI SA features and many work have been carried out based on this property (e.g., Liszt et al. 1981; Jackson et al. 2002; Goldsmith & Li 2005; Busfield et al. 2006; Anderson & Bania 2009; Roman-Duval et al. 2009). The HI SA property also seems effective in resolving kinematic distance ambiguity toward SNR-MC associations, such as 3C 397 (Jiang et al. 2010) and CTB 109 (Tian et al. 2010). Figure 7 (lower panels) shows the VGPS HI and GRS ¹³CO spectra of two regions (as defined in the upper left panel) near the remnant. The HI SA feature is clearly seen at 69 km s⁻¹ associated with the ¹³CO peak, which indicates that the 69 km s⁻¹ molecular component is most probably located at the near distance along the LOS, i.e., 4.3 kpc. This component seems to be a part of the $69.65~\rm km~s^{-1}~MC$ complex GRSMC G039.34-00.26at the near side (Roman-Duval et al. 2009), which is apparently outside the distance range 6.2–12.5 kpc inferred for SNR 3C 396.

Therefore we suggest that SNR 3C 396 is more probably associated with the MCs at $\sim 84 \text{ km s}^{-1}$. The derived column density and gas mass of some molecular features (the northwestern patch, southwestern pillar and the tip, and the western wall (Figure 8)) are pre-

sented in Table 1. In the derivation of these parameters, two methods are used and similar results are yielded. In the first method, the $\rm H_2$ column density is calculated by adopting the mean CO-to-H₂ mass conversion factor $N(\rm H_2)/W(^{12}\rm CO) \approx 1.8 \times 10^{20}~\rm cm^{-2} K^{-1} km^{-1} s$ (Dame et al. 2001). In the second method, on the assumption of local thermodynamic equilibrium and the excitation temperature $\sim 10~\rm K$, the $^{13}\rm CO$ column density is converted to the $\rm H_2$ column density using the relation $N(\rm H_2){=}7\times 10^5 N(^{13}\rm CO)$ (Frerking et al. 1982). Assuming a cuboidal volume for the wall region (Figure 8) with size $4'.5\times 4'.5\times 9'.5$, the mean molecular density of the western wall is inferred as $\sim 170 d_{6.2}^{-1}~\rm H_2~cm^{-3}$.

3.2. X-ray Properties of 3C 396

Next, we investigate the positional relation of SNR 3C 396 X-ray emission with the CO intensity distribution in detail. In general, we extracted *Chandra* X-ray spectra from five X-ray bright regions (as defined in Figure 9) using the CIAO3.4 script *specextract*. The background spectrum was extracted from four nearby regions (dashed circles in Figure 9). The five on-source spectra were adaptively regrouped to achieve a background-subtracted signal-to-noise ratio (S/N) of 5 per bin. Then we used a nonequilibrium ionization (NEI) model to fit the spectra of the remnant. The XSPEC spectral fitting package was used throughout. For the foreground absorption, the cross sections from Morrison & McCammon (1983) were used. The parameters of the fitting are listed in Table 2 with the 90% confidence ranges.

The five spectra all contain distinct lines of Si XIII $(\sim 1.85 \,\mathrm{keV})$ and S XV $(\sim 2.45 \,\mathrm{keV})$, but Ar XVII $(\sim 3.12\,\mathrm{keV})$ and Ca XIX $(\sim 3.86\,\mathrm{keV})$ lines are prominent only in the northern and southern regions (Figure 10). The model of our spectral fit generates a variable hydrogen column density from $4.0 \times 10^{22} \text{ cm}^{-2}$ to 6.5×10^{22} cm⁻². These values are roughly consistent with 4.65×10^{22} cm⁻² from the diffuse X-ray spectral fitting with ASCA X-ray observation (Harrus & Slane 1999) and $5.3\times10^{22}\,\mathrm{cm^{-2}}$ from the entire central nebula spectral fitting with Chandra X-ray observation (Olbert et al. 2003). The northern and southern regions have relatively high temperatures ($\gtrsim 1 \,\mathrm{keV}$) and slight overabundance of Si, S, and Ca. The temperatures of the other three regions are relatively low, around 0.7 keV. The western edge is also S enriched and, notably, only the southwestern region is found to be of normal abundance. The ionization timescales, $n_e t$, in the northern, southern, and western regions are less than 5.5×10^{11} s cm⁻³ but seems to be higher in the southwestern region (> 4×10^{11} s cm⁻³).

An estimate of the hot-gas hydrogen-atom density $n_{\rm X}$ of these regions is made using the volume emission measure, $fn_en_{\rm X}V$, derived from the normalization of the XSPEC model, where n_e is the electron density, V the volume of the emitting region, and f the volume filling factor of the hot-gas (0 < f < 1). Here we have assumed $n_e \approx 1.2n_{\rm X}$ and oblate spheroids for the defined elliptical regions (Figure 9). The derived physical parameters are listed in Table 3. If we adopt $n_{\rm X} = 2f^{-1/2}d_{6.2}^{-1/2}$ cm⁻³ as the mean density of SNR's hot-gas (where $d_{6.2} = d/6.2$ kpc is used for scaling; Section 4.1) and assume an oblate spheroid $(2'.7 \times 3'.9 \times 3'.9)$ for the entire diffuse thermal X-ray emitting volume, $V = 3.0 \times 10^{58} fd_{6.2}^3$ cm³,

the mass of the X-ray emitting hot-gas of SNR 3C 396 is $\sim 70 f^{1/2} d_{6.2}^{5/2} M_{\odot}$. In the Chandra ACIS three-color image (Figure 3, right

In the Chandra ACIS three-color image (Figure 3, right panel), the X-ray emission is hard in the central PWN region and the northern and southern regions (dominated by the blue color), relatively soft along the western boundary (dominated by the green color), and softest in the southwestern edge (seen as an orange patch). This is consistent with the distribution of hot-gas temperatures derived above. The softest patch is coincident with the tip of the $V_{\rm LSR} \sim 84\,{\rm km\,s^{-1}}$ molecular finger/pillar.

4. DISCUSSION

4.1. Association of SNR 3C 396 with the $V_{\rm LSR} \sim \! 84~km~s^{-1}~MCs$ and the Distance

The cavity-like $^{12}\mathrm{CO}$ structure at $V_{\mathrm{LSR}}\sim 69\,\mathrm{km\,s^{-1}}$ seems consistent with the GRS $^{13}\mathrm{CO}$ data (Lee et al. 2009; Figure 7 therein). Based on such a structure at $V_{\mathrm{LSR}}\sim 69\,\mathrm{km\,s^{-1}}$ that seems to roughly surround SNR 3C 396, Lee et al. (2009) suggest an association of 3C 396 with the $\sim 69\,\mathrm{km\,s^{-1}}$ MCs and thus adopt a distance 8.5 kpc. However, the HI SA property of the 69 km s $^{-1}$ molecular component indicates that it is most likely to be in the foreground ($\sim 4.3~\mathrm{kpc}$) toward SNR 3C 396, while the 21 cm HI absorption feature suggests the SNR being located in the distance range 6.2–12.5 kpc (Section 3.1). It thus appears difficult to associate the $\sim 69\,\mathrm{km\,s^{-1}}$ MCs with the remnant. In our $^{12}\mathrm{CO}$ observation, we indeed find that the cavity-like structure of the 69 km s $^{-1}$ molecular component does not well match the morphology of the remnant (Section 3.1).

Besides the 69 km s⁻¹ MCs, however, we have found that the western boundary of the SNR is perfectly confined by the western molecular wall at $V_{\rm LSR} \sim 84\,{\rm km\,s^{-1}}$ and the multiwavelength (X-ray, mid-IR, and radio) properties are consistent with the presence of the $84\,{\rm km\,s^{-1}}$ MCs (Section 3.1).

The eastern ¹²CO patch (seen in Figure 2, at 87–88 km s⁻¹; Figure 4, the right panel in the fourth line) is shown to have a redshifted broadening (87–90 km s⁻¹) in the ¹²CO spectral line profiles (Figure 6, left panel) and thus probably represents the molecular gas perturbed by the SNR. The molecular line broadening has widely been used as a kinematic evidence of interaction between SNR shocks and MCs (see Jiang et al. 2010), such as in the studies of prototype interacting SNRs IC 443 (DeNoyer 1979), W28 (Arikawa et al. 1999), HB21 (Byun et al. 2006), and G347.3-0.5 (Moriguchi et al. 2005). More recently, broadened line profiles of optically thin ¹²CO lines were also successively found in our serial work on SNR–MC interaction (Kes 69, Zhou et al. 2009; Kes 75, Su et al. 2009; and 3C 397, Jiang et al. 2010).

Although the broad blue wings of the $\sim 84\,\mathrm{km\,s^{-1}}$ ¹²CO lines of the western region of 3C 396 cannot be exclusively determined to be dynamically broadened profiles (Section 3.1; Figure 6, right panel), the relatively enhanced ¹²CO J=2-1/J=1-0 ratios in such wings (80–83 km s⁻¹) in the northwestern and southwestern boundaries (Figure 5, lower left panel) coincide with the southwestern molecular intrusion region and the northwestern molecular patch, and also with two radio brightness peaks, respectively, which is in favor of a perturbation

of the western molecular gas by the SNR expansion. We note that the maximum ratio obtained here is not higher than 1, while higher values are observed in other interacting SNRs (e.g., W44, IC 443, HB21, G349.7+0.2, and G18.8+0.3, see Dubner et al. 2004 and references therein). Two main reasons may explain why the ratio value in 80–83 km s⁻¹ interval does not exceed unity: 1. The filling factor of the disturbed ^{12}CO (J=2-1) emitting region may be small in the 48" beam size in 3C 396 compared to that for ^{12}CO (J=1-0), and the line ratios could thus be diluted. 2. The location of 3C 396 at the tangent point makes the environment much complicated and may cause unignorable velocity crowding in the interval of interest, with the line wings difficult to differentiate. Actually, e.g., there is a distinct cloud represented by the ¹³CO line peak at 81 km s⁻¹ in the southwestern molecular intrusion region (see Figure 6, right panel). Confusion of the ¹²CO emission of such gas will decrease the $^{12}CO J = 2-1/J = 1-0$ ratios in the velocity interval.

In multiwavelength morphologies, both the X-ray and radio emissions are bright in the western half and faint in the eastern half (Figures 3 and 9), which is probably because of the large-scale density gradient roughly perpendicular to the Galactic plane. The bright side of the remnant is close to the Galactic plane (see Figure 7, upper left panel, in Galactic coordinates). The bright X-ray, IR and radio emissions in the west are well confined by the thick molecular wall of the $\sim 84~{\rm km~s^{-1}}$ component, which may suggest that the SNR expansion is hampered there. This scenario is strengthened by the radio and IR brightness peaks and the soft Xray patch in the southwestern edge, which are coincident with the "tip" of the intruding finger/pillar of molecular gas. When the SNR shock hits the dense molecular pillar or clumps, it will be decelerated and thus the magnetic field be compressed and amplified. This can account for the prominent radio enhancement and sharp edge there. Actually, the magnetic field in the SW of the remnant is found to be essentially tangential to the shell, which is probably because the random interstellar magnetic field has been chiefly swept up into the accumulated gas and compressed along with the remnant's shell (Patnaik et al. 1990). [Parenthetically, the tangential field (Patnaik et al. 1990) and the slightly enhanced radio emission in the northwestern edge are consistent with the presence of the dense molecular clump in the NW (Section 3.1).] In Xrays, the low electron temperature, normal metal abundance, and large ionization timescale (as obtained from our spectral fitting) of the soft southwestern X-ray patch can be naturally interpreted by the interaction with the dense molecular pillar. The IR morphology can also be accounted for with the scenario of shock interaction with western molecular gas, as discussed in the following.

In IR, there is a spatial separation between the inner near-IR 1.64 μ m [FeII] and outer 2.12 μ m H₂ emission filaments along the western edge of the remnant (Lee et al. 2009; Hewitt et al. 2009). Lee et al. (2009) interprets this morphology due to the SNR shock overtaking the wind of a red supergiant (RSG), giving rise to [FeII] emission and the interaction with a dense circumstellar bubble, giving rise to H₂ emission. Such a RSG wind bubble 5–7 pc in radius invokes a 25–35 M_{\odot} progenitor. This mass assumption is different from our estimate of 13–15 M_{\odot}

derived from the X-ray emitting metal abundances (see below in Section 4.2.3) and is not in agreement with the mass range $\lesssim 25 M_{\odot}$ calculated for the neutron star progenitors with metallicity $Z \lesssim Z_{\odot}$ (Heger et al. 2003). The $13-15 M_{\odot}$ progenitor of type-IIP supernova (see Section 4.2.3) can only blow a RSG wind bubble of radius $\lesssim 1$ pc (Chevalier 2005). However, the spatially separated [FeII] and H₂ emission can be interpreted in term of SNR–MC interaction. As Reach et al. (2005) and Hewitt et al. (2009) suggest, the H₂ emission can arise from the shock interaction with dense clumps while the [FeII] emission can arise from the same shock encountering the less dense material at the clumps' surface or from the ejecta.

The bright 24 μ m mid-IR emission (Figure 3) may chiefly come from the dust grains and even possibly from the ionic and molecular species in the shocked gas (e.g., Tappe et al. 2006; Su & Chen 2008) when the western molecular wall is hit by the blast wave. A spinning dust component is invoked to account for the spectral excess at 33 GHz (Scaife et al. 2007), and it seems that the needed dust may lie in the MCs and be heated by the shocked gas.

All these evidences strongly point to a conclusion that SNR 3C 396 is associated, and in physical contact, with the $\sim 84\,\mathrm{km\,s^{-1}}$ MCs. The LSR velocity 84 km s⁻¹ corresponds to a Galactic location near the tangent point, at a distance of ~ 6.2 kpc; this distance is consistent with the range [6.2–12.5 kpc (Section 3.1)] inferred from the HI absorption data. We also notice that a distance of 6.5 kpc suggested by Hewitt et al. (2009) based on the hydrogen column is very similar to our result. Hereafter, we write the distance to 3C 396 as $d=6.2d_{6.2}\,\mathrm{kpc}$ for scaling.

It was queried by Patnaik et al. (1990) whether the HII complex NRAO 591 (or U39.25–0.07), which looks projectively near 3C396, is associated with the SNR. Since the complex is at $V_{\rm LSR}=23~{\rm km~s^{-1}}$ with the far side distance of 12.1 kpc (Anderson & Bania 2009), it is not associated with the remnant. Instead, it is very likely to be associated with the 22.46 km s⁻¹ GRSMC G039.24–00.06 at the far side (Roman-Duval et al. 2009).

4.2. SNR physics of 3C 396 4.2.1. Global evolution

According the above multiwavelength analysis, a general scenario for SNR 3C396 can be established as this: the remnant collides with a molecular wall in the west, flanking a southwestern pillar of molecular gas, and expands in a low density region in the east (but encountering a clump of backside molecular gas).

The global dynamical evolution of the remnant can be inferred from the X-ray properties. Adopting $kT_{\rm X}\sim 0.9$ keV as the average postshock temperature in the interclump medium, we have the mean blast shock velocity $v_s = [16kT_{\rm X}/(3\bar{\mu}m_{\rm H})]^{1/2} \sim 8.7 \times 10^2$ km s⁻¹, where $m_{\rm H}$ is the hydrogen atom mass and $\bar{\mu}=0.61$ is the average atomic weight. Assuming an adiabatic expansion and adopting the SNR radius $r_s \sim 3'.9 \sim 7.0 d_{6.2}$ pc and the mean density of the interclump medium $n_0 \sim n_{\rm X}/4 \sim 1f^{-1/2}d_{6.2}^{-1/2}$ cm⁻³, the SNR's age is estimated as $t=(2r_s)/(5v_s) \sim 3d_{6.2}$ kyr and the explosion energy is $E=(25/4\xi)(1.4n_0m_{\rm H})v_s^2r_s^3 \sim 6(n_0/1\,{\rm cm}^{-3})\times 10^{-10}$

 $10^{50}d_{6.2}^{5/2}$ erg (where $\xi=2.026$). The dynamical age estimated here is consistent to the ionization ages (the time since passage of the shock wave) of the X-ray emitting gas obtained from the spectral fit (Table 3), except the region "W" for which the ionization age seems relatively low.

4.2.2. Pressure discrepancy

The thermal pressure of the X-ray emitting gas is about $p_{\rm h} \sim 1 \times 10^{-8} f^{-1/2} d_{\rm 6.2}^{-1/2}$ dynes cm⁻² (Table 3), which is about two order of magnitudes lower than that of the shock ram pressure $p_{\rm cl} \sim 3 \times 10^{-6}$ dynes cm⁻², as derived from the H₂ emission of the Spitzer IRS observation towards the southwestern region (Hewitt et al. 2009). Similar pressure discrepancies have also been found in the cases of IC 443 (Moorhouse et al. 1991) and 3C 391 (Reach & Rho 1999). Such discrepancies can be explained if the western molecular gas is clumpy and there is a radiative shell between the hot gas and the dense molecular clumps (Chevalier 1999). A radiative shock has been revealed by the Spitzer IRS slit observation (Hewitt et al. 2009). On the assumption of a crude pressure balance between the hot gas and the radiative shell, we have (Chevalier 1999)

$$rac{p_{
m cl}}{p_{
m h}} \sim rac{n_{
m cl}}{n_0} \left[1 + \left(rac{n_{
m cl}}{n_{
m rs}}
ight)^{1/2}
ight]^{-2},$$

where $n_{\rm cl}$ is the hydrogen atom density in the clump, n_0 the interclump density, and $n_{\rm rs}$ the density in the radiative shell. The gas density in the dense clump, $n_{\rm cl} \sim 1 \times 10^4 \, {\rm cm}^{-3}$, was estimated for the southwestern region from the H₂ lines by two groups of authors (Lee et al. 2009; Hewitt et al. 2009). Considering that the X-ray emission represents the shock interaction with the interclump gas, we may assume n_0 is about 1/4 the density of the hot gas ($n_{\rm X}$, see Table 3) and thus is of order 1 cm⁻³ for the southwestern region. Hence we obtain $n_{\rm rs} \sim 4 \times 10^2 \, {\rm cm}^{-3}$. This number is similar to the electronic density ($\sim 3 \times 10^2 \, {\rm cm}^{-3}$) inferred from ionic lines (Hewitt et al. 2009).

4.2.3. Supernova ejecta and progenitor

In the north and south, the $\sim 84\,\mathrm{km\,s^{-1}}$ CO emission is very weak, the SNR does not seem to encounter the molecular wall, and the X-ray emitting gas is found to be metal enriched (Table 2). We assume that the observed pattern of metal enrichment can reflect the composition of the supernova ejecta and thus be used to constrain the mass of the progenitor star (following, e.g., Rakowski et al. 2001; Chen et al. 2006). As the presence of a pulsar implies a core-collapse nature of the SN, we plot the relative metal abundances predicted from such SN models for stars with normal metallicities $(Z = Z_{\odot})$ (Thielemann, Nomoto, & Hashimoto 1996, hereafter TNH96; Woosley & Weaver 1995, hereafter WW95) in Figure 11. The enrichment appears compatible with the WW95 model for a progenitor mass of $M=15M_{\odot}$ or the TNH96 model for a progenitor mass of $M=13M_{\odot}$. A 13–15 M_{\odot} progenitor is a B1-B2 star (Snow 1982) and ends its life as a type-IIP supernova (Heger et al. 2003).

5. CONCLUSIONS

We have investigated the molecular gas environment of the semicircular young composite SNR 3C 396 in multi-wavelengths, principally with 12 CO (J=1–0 and J=2–1) and 13 CO (J=1–0) observations in SRAO and PMOD, and performed a *Chandra* spatially resolved thermal X-ray spectroscopic study of the SNR. The main conclusions are summarized as follows.

- 1. We confirmed a cavity-like structure of molecular gas at $\sim 67-72\,\mathrm{km\,s^{-1}}$ in the 3C 396 SNR region, which was noticed by Lee et al. (2009) based on the GRS $^{13}\mathrm{CO}$ ($J{=}1{-}0$) data. It is most probably to be located in the near distance ($\sim 4.3~\mathrm{kpc}$) according to the HI SA measurement.
- 2. We find a series of evidence suggesting that the molecular gas at \sim 84 km $\rm s^{-1}$ is in physical contact with SNR 3C 396, which can reasonably explain the multiwavelength properties of the remnant. Around this LSR velocity, a molecular wall appears to perfectly confine the western boundary of the SNR, which is bright in X-ray, IR, and radio emission. The CO emission fades out from west to east, indicating that the eastern region is of low gas density, accounting for the radio "blow-out" morphology in the east of the remnant. A molecular pillar is revealed in the SW, with one end intruding inside the SNR border. The shock interaction with this "pillar tip" can explain the X-ray and radio enhancement in the SW and some infrared filaments there. The SNR-MC interaction is also favored by the relatively elevated 12 CO J=2-1/J=1-0 line ratios at $80-83\,\mathrm{km\,s^{-1}}$ in the southwestern "tip" and the molecular patch on the northwestern boundary. Redshifted broadening (86–90 km s⁻¹) is detected in the ¹²CO spectral line profiles of the eastern 81 km s⁻¹ molecular patch and may be the kinematic evidence for shock-MC interaction.
- 3. The establishment of the association between 3C 396 and the 84 km s $^{-1}$ MCs results in a determination of the kinematic distance at $\sim 6.2\,\mathrm{kpc}$ to the remnant, which agrees with a location at the tangent point along the LOS.
- 4. The diffuse thermal X-ray emitting gas is found to be metal enriched except in the southwestern X-ray enhancement, and the metal enrichment in the north and south implies that the supernova progenitor is a 13–15 M_{\odot} B1–B2 star.
- 5. The X-ray spectral analysis suggests an age of the remnant of ~ 3 kyr. There is a pressure discrepacy between the X-ray emitting gas and the IR emitting cloud shock in the west, which can be explained with the inhomogeneous molecular gas and radiative shells between the hot gas and the dense molecular clumps.

The authors are thankful to the staff members of the SRAO and the Qinghai Radio Observing Station at Delingha for their support in observation and to Lawrence Rudnick for providing the VLA data of SNR 3C 396. We

TABLE 1 Parameters of the $\sim 84\,\mathrm{km}\,\mathrm{s}^{-1}$ Molecular Gas

Region ^a	$N({\rm H_2})(10^{21}{\rm cm^{-2}})^{\rm b}$	$M(M_{\odot})^{ m b}$
Northwestern clump	4.4/4.1	$\begin{array}{c} 1.9 \times 10^3 d_{6,2}^2 / 1.8 \times 10^3 d_{6,2}^2 \\ 3.7 \times 10^3 d_{6,2}^2 / 3.6 \times 10^3 d_{6,2}^2 \end{array}$
Pillar	4.6/4.5	$3.7 \times 10^3 d_{6.2}^{3.2} / 3.6 \times 10^3 d_{6.2}^{3.2}$
Pillar tip	4.3/4.4	$6.9 \times 10^2 d_{6.2}^{3.2} / 7.1 \times 10^2 d_{6.2}^{3.2}$
Western wall	4.2/3.8	$6.9 \times 10^2 d_{6.2}^{3.27} / 7.1 \times 10^2 d_{6.2}^{3.2} $ $1.3 \times 10^4 d_{6.2}^2 / 1.2 \times 10^4 d_{6.2}^2$

^a Regions are defined in Figure 8.

acknowledge the use of the VGPS and GRS data; the National Radio Astronomy Observatory is a facility of the National Science Foundation operated under cooperative

agreement by Associated Universities, Inc. This work is supported by the NSFC grants 10621303, 10673003, and 10725312 and the 973 Program grant 2009CB824800.

REFERENCES

Anderson, L. D., & Bania, T. M. 2009, ApJ, 690, 706 Anderson, M. C., & Rudnick, L. 1993, ApJ, 408, 514

Arikawa, Y., Tatematsu, K., Sekimoto, Y., & Takahashi, T. 1999, PASJ, 51, L7

Becker, R. H., & Helfand, D. J. 1987, AJ, 94, 1629

Busfield, A. L., Purcell, C. R., Hoare, M. G., Lumsden, S. L., Moore, T. J. T., & Oudmaijer, R. D. 2006, MNRAS, 366, 1096 Byun, D.-Y., Koo, B.-C., Tatematsu, K., & Sunada, K. 2006, ApJ, 637, 283

Chen, Y., Wang, Q. D., Gotthelf, E. V., Jiang, B., Chu, Y. H., & Gruendl, R. 2001, ApJ, 651, 237

Chevalier, R. A. 1999, ApJ, 511, 798

Chevalier, R. A. 2005, ApJ, 619, 839

Clemens, D. P. 1985, ApJ, 295, 422

Dame, T. M., Hartmann, D., & Thaddeus, P. 2001, ApJ, 547, 792 DeNoyer, L. K. 1979, ApJ, 232, L165

Dubner, G., Giacani, E., Reynoso, E., & Paron, S. 2004, A&A,

Frerking, M. A., Langer, W.D., & Wilson, R. W. 1982, ApJ, 262,

Goldsmith, P. F., & Li, D. 2005, ApJ, 622, 938

Harrus, I. M., & Slane, P. O. 1999, ApJ, 516, 811 Heger, A., Fryer, C. L., Woosley, S. E., Langer, N., &

Hartmann, D. H. 2003, ApJ, 591, 288 Hewitt, J. W., Yusef-Zadeh, F., Wardle, M., Roberts, D. A., &

Kassim, N. E. 2006, ApJ, 652, 1288

Hewitt, J. W., Rho, J., Andersen, M., & Reach, W. T. 2009, ApJ, 694, 1266

Jackson, J. M., Bania, T. M., Simon, R., Kolpak, M., Clemens, D. P., & Heyer, M. 2002, ApJ, 566, L81

Jackson, J. M., Rathborne, J. M., Shah, R. Y., Simon, R., Bania, T. M., Clemens, D. P., Chambers, E. T., Johnson, A. M., Dormody, M., Lavoie, R., & Heyer, M. H. 2006, ApJS, 163, 145

Jiang, B., Chen, Y., Wang, J. Z., Su, Y., Zhou, X., Safi-Hard, S., & DeLaney, T. 2010, ApJ, 712, 1147

Landecker, T. L., Routledge, D., Reynolds, S. P., Snegal, R. J., Borkowski, K. J., & Seward, F. D. 1999, ApJ, 527, 866

Lee, H.-G., Moon, D.-S., Koo, B.-C., Lee, J.-J., & Matthews, K. 2009, ApJ, 691, 1042

Liszt, H. S., Burton, W. B., & Bania, T. M. 1981, ApJ, 246, 74 Moorhouse, A., Brand, P. W. J. L., Geballe, T. R., & Burton, M. G. 1991, MNRAS, 253, 662

Moriguchi, Y., Tamura, K., Tawara, Y., Sasago, H., Yamaoka, K., Onishi, T., & Fukui, Y. 2005, ApJ, 631, 947

Morrison, R., & McCammon, D. 1983, ApJ, 270, 119

Olbert, C. M., Keohane, J. W., Arnaud, K. A., Dyer, K. K., Reynolds, S. P., & Safi-Harb, S. 2003, ApJ, 592, L45

Patnaik, A. R., Hunt, G. C., Salter, C. J., Shaver, P. A., & Velusamy, T. 1990, A&A, 232, 467

Rakowski, C. E., Hughes, J.P., & Slane, P. 2001, ApJ, 548, 258

Reach, W. T., & Rho, J. 1999, ApJ, 511, 836

Reach, W. T., Rho, J., & Jarrett, T. H. 2005, ApJ, 618, 297 Reid, M. J. 1993, ARA&A, 31, 345

Rieke, G. H. et al. 2004, ApJS, 154, 25

Roman-Duval, J., Jackson, J. M., Heyer, M., Johnson, A., Rathborne, J., Shah, R., & Simon, R. 2009, ApJ, 699, 1153

Scaife, A. et al. 2007, MNRAS, 377, L69

Seta, M., Hasegawa, T., Dame, T. M., Sakamoto, S., Oka, T., Handa, T., Hayashi, M., Morino, J.-I., Sorai, K., & Usuda, K.S. 1998, ApJ, 505, 286

Snow, T. P., Jr. 1982, ApJ, 253, L39 Stil, J. M., Taylor, A. R., Dickey, J. M., Kavars, D. W., Martin, P. G., Rothwell, T. A., Boothroyd, A. I., Lockman, F. J., & McClure-Griffiths, N. M. 2006, AJ, 132, 1158 Su, Y., & Chen, Y. 2008, AdSpR, 41, 401

Su, Y., Chen, Y., Yang, J., Koo, B.-C., Zhou, X., Jeong, I.-G., & Zhang, C.-G. 2009, ApJ, 694, 376

Tappe, A., Rho, J., & Reach, W. T. 2006, ApJ, 653, 267 Taylor, J. H., & Cordes, J. M. 1993, ApJ, 411, 674

Thielemann, F.-K, Nomoto, K., & Hashimoto, M-A. 1996, ApJ,

Tian, W. W., Leahy, D. A., & Wang, Q. D. 2007, A&A, 474, 541 Tian, W. W., Leahy, D. A., & Li, D. 2010, MNRAS, 404, L1 van Dishoeck, E. F., Jansen, D. J., & Phillips, T. G. 1993, A&A, 279, 541

Woosley, S. E. & Weaver, T. A. 1995, ApJS, 101, 181 Zhou, X., Chen, Y., Su, Y., & Yang, J. 2009, ApJ, 691, 516

^b See text for the two methods used for the column density derivation.

TABLE 2 Chandra X-ray Spectral Fits with 90% Confidence Ranges

Region	N	W	SW	S	E	N+S
$N_{\rm H}(10^{22}{\rm cm}^{-2})$	$4.84^{+0.30}_{-0.13}$	$5.50^{+0.97}_{-0.92}$	$4.42^{+0.41}_{-0.39}$	$4.74^{+0.26}_{-0.33}$	$4.95^{+1.10}_{-0.83}$	$4.82^{+0.21}_{-0.20}$
$kT_{ m X}({ m keV})$	$1.33^{+0.20}_{-0.19}$ $1.66^{+0.28}_{-0.27}$	$0.71^{+0.25}_{-0.15}$	$0.66^{+0.10}_{-0.08}$	$1.04^{+0.11}_{-0.14}$	$0.68^{+0.37}_{-0.19}$	$1.21^{+0.13}_{-0.13}$
Si	$1.66^{+0.28}_{-0.27}$	$0.92^{+0.31}_{-0.23}$	$_{1.09}\pm 0.23$	$1.42^{+0.36}_{-0.27}$	1^{a}	$1.56^{+0.21}_{-0.21}$
\mathbf{S}	$1.66_{-0.27}^{+0.27}$ $1.73_{-0.27}^{+0.29}$	$0.92_{-0.23}^{+0.31} \\ 1.99_{-0.67}^{+0.77}$	$1.23_{-0.24}^{+0.32} \\ 1.20_{-0.28}^{+0.32}$	$1.60^{+0.40}_{-0.27}$	1^{a}	$1.21_{-0.13}^{+0.13}$ $1.56_{-0.21}^{+0.21}$ $1.63_{-0.21}^{+0.22}$
Ca	$1.91^{+1.16}_{-0.86}$	1^{a}	1^{a}	$3.08^{+1.93}_{-1.45}$	1^{a}	$1.98^{+0.93}_{-0.86}$
$\tau(10^{11} {\rm s~cm^{-3}})$	$2.19_{-0.63}^{+1.50}$ $1.26_{-0.39}^{+0.48}$	$0.42^{+0.46}_{-0.10}$	>4.06	$2.69^{+2.79}_{-1.09}$	>0.84	$2.34^{+1.29}_{-0.74}$
$fn_e n_{\rm X} V/d_{\rm 6.2}^2 (10^{57} {\rm cm}^{-3})$	$1.26^{+0.48}_{-0.39}$	$\begin{array}{c} 0.42 \begin{array}{c} -0.10 \\ -0.10 \end{array} \\ 2.73 \begin{array}{c} +4.32 \\ -2.73 \end{array}$	$2.35^{+1.55}_{-0.88}$	$1.28^{+0.52}_{-0.38}$	$2.34^{+0.63}_{-2.34}$	$2.50^{+0.71}_{-0.52}$
$fn_e n_{\rm X} V/d_{6.2}^2 (10^{57} {\rm cm}^{-3}) $ $\chi_r^2 ({\rm dof})$	1.27(78)	1.21(28)	0.66(48)	1.40(59)	1.14(19)	1.54(101)

^a Fixed to the solar abundance.

TABLE 3 PARAMETERS OF THE HOT GAS

Region	N	W	SW	S	E
Volume $(10^{56}fd_{6.2}^3~{ m cm}^3)^{ m a,b}$ $n_{ m X}(f^{-1/2}d_{6.2}^{-1/2}~{ m cm}^{-3})$ ${ m Mass}(f^{1/2}d_{6.2}^{5/2}~{ m M}_{\odot})$	10.1	4.4	1.8	3.5	14.5
$n_{\rm X}(f^{-1/2}d_{6.2}^{-1/2}~{ m cm}^{-3})$	1.0	2.3	3.3	1.7	1.2
$Mass(f^{1/2}d_{6,2}^{5/2}M_{\odot})$	1.2	1.2	0.7	0.7	2.0
Ionization Age $(10^3 f^{1/2} d_{e,2}^{1/2} \text{ yr})$	5.6	0.5	> 3.2	4.0	> 1.9
Pressure($10^{-9}f^{-1/2}d_{6.2}^{-1/2}$ dynes cm ⁻²)	6.1	7.3	9.7	8.1	3.5

^a Here f is the filling factor of the X-ray emitting gas and $d_{6.2}$ is the distance to the remnant in units of 6.2 kpc (Section 4.1). ^b In the estimate of the volumes, we assume the oblate spheroids for elliptical regions N, W, SW, S, and E, with half axes $0'.88 \times 1'.26 \times 1'.26$, $0'.49 \times 1'.11 \times 1'.11$, $0'.63 \times 0'.63 \times 0'.63 \times 0'.63 \times 0'.91 \times 0'.91$, and $1'.01 \times 1'.41 \times 1'.41$, respectively.

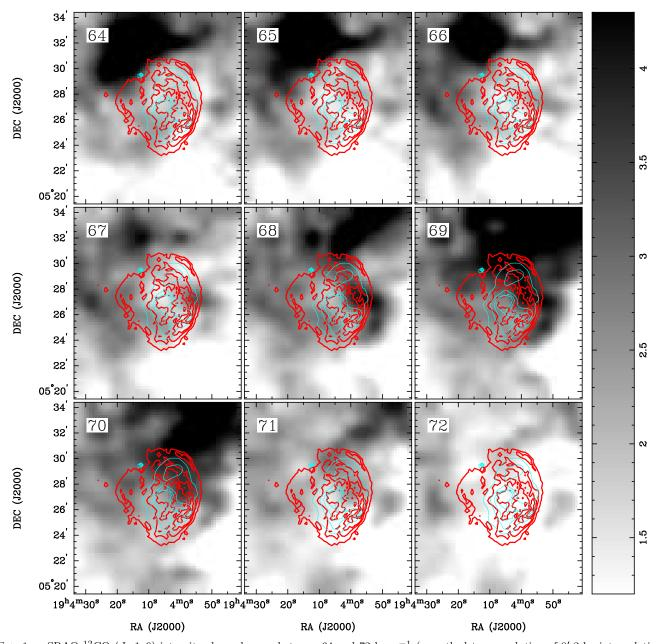


Fig. 1.— SRAO 12 CO (J=1–0) intensity channel maps between 64 and 72 km s $^{-1}$ (smoothed to a resolution of 0′.2 by interpolation), overlaid with the 1.0–7.0 keV X-ray (cyan, thin) contours and the 1.4 GHz radio (red, thick) continuum emission contours at levels of 1.5, 3.5, 5.5, 7.5, 9.5 mJy beam $^{-1}$.

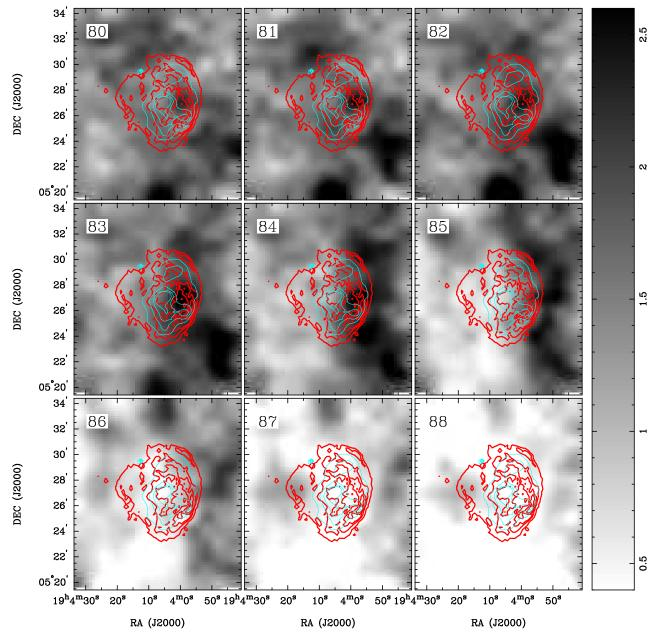


Fig. 2.— SRAO 12 CO (J=1–0) intensity channel maps between 80 and 88 km s $^{-1}$ (smoothed to a resolution of 0'.2 by interpolation), overlaid with the 1.0–7.0 keV X-ray (cyan, thin) contours and the 1.4 GHz radio (red, thick) continuum emission contours at the same levels as in Figure 1.

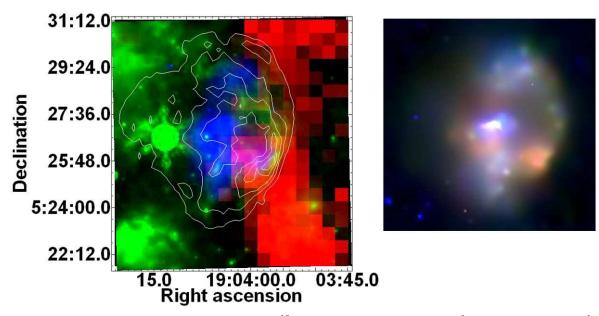


Fig. 3.— Left: multiband image of SNR 3C 396. The PMOD 12 CO intensity map (> 2.2 K km s $^{-1}$ or $^{11}\sigma$) in 85–88 km s $^{-1}$ interval is in red, the Spitzer 24 μ m mid-IR emission in green, and the Chandra 1.0–7.0 keV X-rays (adaptively smoothed with the CIAO program csmooth to achieve a S/N ratio of 3) in blue. Each of the intensity maps is in logarithmic scale. The five levels of the VLA 1.4 GHz contours are linear between the 78.6% and 12.4% maximum brightness. Right: Chandra ACIS X-ray tri-color image of SNR 3C 396. The Si (1.65–2.1 keV) is in red, the S (2.25–2.6 keV) in green, and the hard continuum (3.0–7.0 keV) in blue.

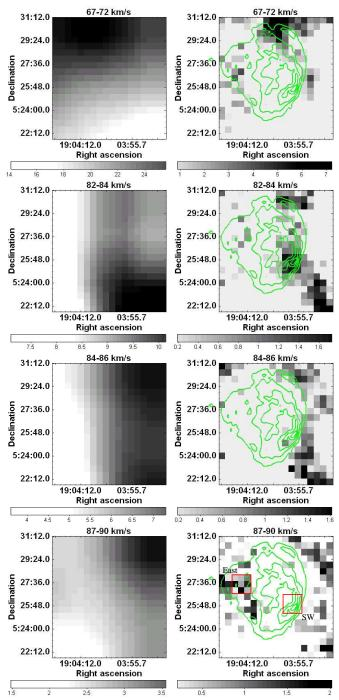


Fig. 4.— The four left panels: the PMOD 12 CO intensity maps in the intervals of 67–72, 82–84, 84–86, and 87–90 km s $^{-1}$, smoothed to 2' to illustrate the large-scale confusion in this direction. The four right panels: the PMOD 12 CO maps in the same velocity intervals after unsharp masking (see text in Section 3.1), overlaid by VLA 1.4 GHz contours at the same levels as in Figure 3.

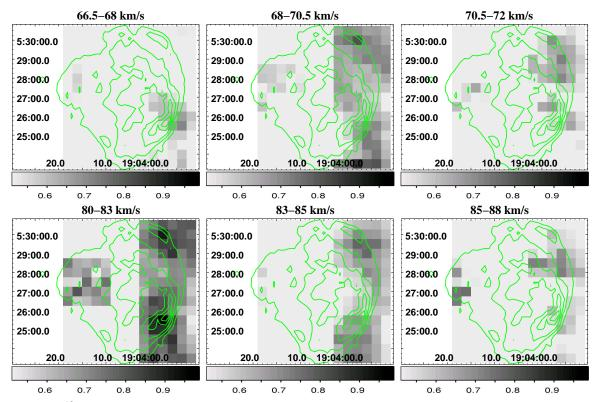


FIG. 5.— Maps of 12 CO J=2-1/J=1-0 intensity ratio around the SNR 3C 396 at velocity ranges 66.5–68, 68–70.5, 70.5–72, 80–83, 83–85, and 85–88 km s⁻¹ after convolving the SRAO 12 CO (J=2-1) data to the same beam size as the PMOD 12 CO (J=1-0) data. Contours show the VLA 1.4 GHz emission at the same levels as in Figure 3.

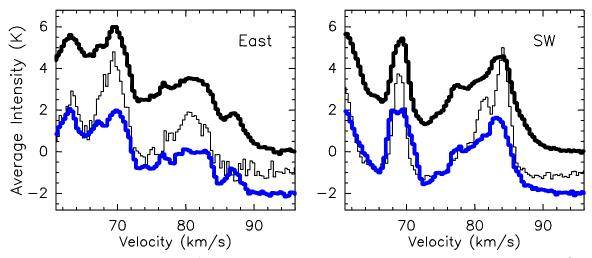


FIG. 6.— The CO spectra in 61–96 km s⁻¹ interval for the eastern [the "East" region in Figure 4, 2.25 arcmin² centered at $(19^{\rm h}04^{\rm m}14^{\rm s},05^{\circ}27'30'')$] and the southwestern [the "SW" region in Figure 4, 2.25 arcmin² centered at $(19^{\rm h}03^{\rm m}58^{\rm s},05^{\circ}25'30'')$] regions of SNR 3C 396. The thick *black*, thick *blue*, and thin lines are for the PMOD 12 CO (J=1-0), SRAO 12 CO (J=2-1), and PMOD 13 CO (J=1-0) (multiplied by a factor of 4) emission, respectively. The profiles of 13 CO (J=1-0) and 12 CO (J=2-1) are shifted by -1 and -2 K, respectively. The 12 CO (J=2-1) spectra are not convolved from beam size 48'' to the 12 CO (J=1-0) beam size 54''.

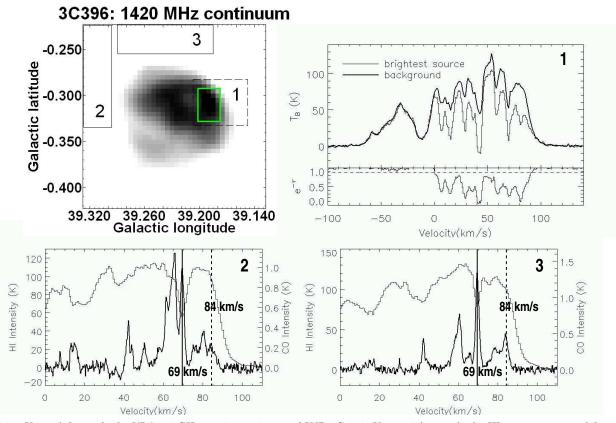


Fig. 7.— Upper left panel: the VLA 1.4 GHz continuum image of SNR 3C 396. Upper right panel: the HI spectra extracted from box 1. The HI spectrum of the bright source is from the solid-line box area, and the background spectrum is from the dashed-line box excluding the solid box area. The dashed line indicates 5 σ derivation for velocities $-100 \leqslant V_{\rm LSR} \leqslant -50$ km s⁻¹ and $110 \leqslant V_{\rm LSR} \leqslant 140$ km s⁻¹. Lower panels: the VGPS HI (thin) and GRS ¹³CO (thick) spectra extracted from boxes 2 and 3 (see the upper left panel), respectively. The vertical solid and dashed lines indicate the position of 69 and 84 km s⁻¹, respectively.

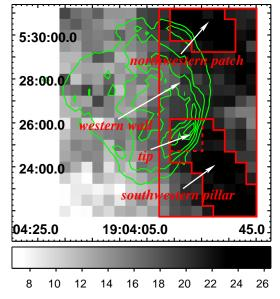


Fig. 8.— PMOD 12 CO intensity map in 82–90 km s $^{-1}$ interval, labelled with the defined regions for the parameter derivation of the 84 km s $^{-1}$ molecular gas. Contours show the 1.4 GHz radio continuum emission towards the remnant at the same levels as in Figure 3.

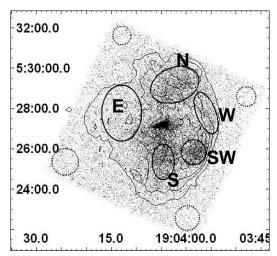
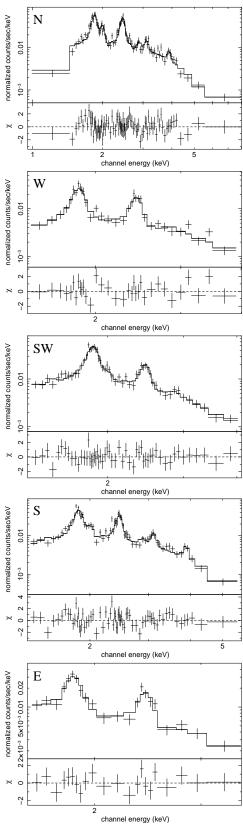


Fig. 9.— Chandra X-ray raw image of SNR 3C 396, labelled with the solid (dotted) defined regions for the source (background) X-ray spectrum extraction. The point sources (except the central pulsar) detected with a wavelet source-detection algorithm have been removed. The contours are the VLA 1.4 GHz radio continuum emission at the same levels as in Figure 3.



 $Fig. \ 10. - Chandra \ ACIS \ X-ray \ spectra \ of the \ SNR \ 3C \ 396 \ (taken \ from \ a \ 93.7 \ ks \ data), \ fitted \ with \ the \ \textit{unei} \ model.$

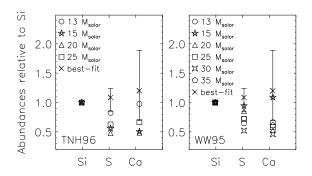


Fig. 11.— The best-fit abundances of the X-ray emitting gas in the north and south (the "N+S" column in Table 2) relative to Si, compared with the predictions from core-collapsed SN models (TNH96 and WW95).